AGU PUBLICATIONS

JGR

Journal of Geophysical Research: Solid Earth

RESEARCH ARTICLE

10.1002/2016JB013155

Key Points:
- The thermoelasticity of Fe_7C_3 was calculated using AIMD under the Earth's inner core conditions
- The elastic properties of Fe_7C_3 agree well with those from seismology due to significant premelting effects
- Fe_7C_3 cannot be the major component of the Earth's core due to its low density

Supporting Information:
- Supporting Information S1

Correspondence to:
Y. Li,
yunguo.li@ucl.ac.uk

Citation:
Li, Y., L. Vočadlo, J. Brodholt, and I. G. Wood (2016), Thermoelasticity of Fe_7C_3 under inner core conditions, *J. Geophys. Res. Solid Earth*, *121*, 5828–5837, doi:10.1002/2016JB013155.

Received 6 MAY 2016
Accepted 14 JUL 2016
Accepted article online 15 JUL 2016
Published online 4 AUG 2016

Thermoelasticity of Fe_7C_3 under inner core conditions

Y. Li[1], L. Vočadlo[1], J. Brodholt[1], and I. G. Wood[1]

[1]Department of Earth Sciences, University College London, London, UK

Abstract It has recently been reported, on the basis of extrapolated experimental data, that the iron carbide, Fe_7C_3, has shear wave velocities and a Poisson's ratio consistent with the seismological values for the Earth's inner core and thus that Fe_7C_3 is a strong candidate for the inner core composition. In this study, using ab initio molecular dynamics simulations, we report the thermoelastic properties of Fe_7C_3 at 350 GPa up to its melting temperature. Due to significant elastic softening prior to melting, the calculated elastic properties, including wave velocities, do indeed agree well with those from seismology. However, the density was found to be much too low (by ~8%) when compared to geophysical data, and therefore, Fe_7C_3 must be ruled out as a major component of the Earth's inner core.

1. Introduction

The primary constituent of the Earth's core is generally accepted to be an iron alloy [*Birch*, 1952; *Allègre et al*., 1995; *McDonough and Sun*, 1995], but the exact composition and structure remain unknown [*Badro et al*., 2014; *Alfè et al*., 2007]. In particular, the compressional (*P* wave, V_P) and shear (*S* wave, V_S) wave velocities from seismic observations are low when compared to observations from mineral physics [e.g., *Vočadlo*, 2007; *Vočadlo et al*., 2009; *Belonoshko et al*., 2007; *Martorell et al*., 2013a]. This makes even a basic understanding of the inner core difficult, let alone the interpretation of the far more complex characteristics of the inner core revealed by recent studies [*Alboussière et al*., 2010; *Olson and Deguen*, 2012; *Tkalčić*, 2015; *Wang et al*., 2015].

A possible explanation for the observed low shear wave velocities when compared with previous mineral physics results was suggested by *Martorell et al*. [2013b] who reported a strong nonlinear shear weakening of pure iron at 360 GPa just before melting ($T/T_m > 0.96$) in the temperature regime expected in the inner core. However, although the low seismic wave velocities of the core could be successfully explained in this way, the density of pure iron was, of course, still too high (by 2–3%) to match the geophysical data. As was made clear by *Martorell et al*. [2013b], a light element component was still required in the inner core to account for this density difference.

The likely candidate light elements for the core, within cosmochemical and petrological constraints, include oxygen, carbon, hydrogen, silicon, and sulfur [*Poirier*, 1994; *Hillgren et al*., 2000]. There is much literature on the subject, published over many years, some of which is contradictory, probably due to the different methodologies, approximations, and interpretations used in the different studies. For example, using density functional theory (DFT), *Alfè et al*. [2002] calculated the chemical potentials of the leading candidate light elements (S, Si, and O) under thermodynamic equilibrium at inner core boundary (ICB) conditions and found S and Si partitioned similarly between the inner and outer core, while oxygen only partitioned into the outer core. In contrast, based on shock wave data, *Huang et al*. [2011] compared the density and sound velocities from geophysics with those in the Fe-O-S system and concluded that oxygen could be ruled out as a major outer core alloying element. *Badro et al*. [2014], however, found that oxygen is always required in the outer core and likely to be at high concentrations. For carbon, *Wood et al*. [2013] used four approaches to obtain a likely upper carbon concentration of ~1 wt % as a component in the whole core. Studies of the iron carbide Fe_7C_3 (see below) suggest that carbon in the form of Fe_7C_3 (8.4 wt %) can indeed match the seismic data. The Fe_7C_3 composition is likely to be the first phase crystallizing from a liquid iron-carbon alloy [*Nakajima et al*., 2009; *Lord et al*., 2009], and from extrapolations of experimental data, it has also been reported that the density of Fe_7C_3 matches well with the inner core under the relevant conditions [*Chen et al*., 2012; *Nakajima et al*., 2011; *Chen et al*., 2014]. Very recently, *Prescher et al*. [2015] further claimed that Fe_7C_3 exhibits a lower shear wave velocity than pure iron and a Poisson's ratio similar to that of the Earth's inner core.

These previous results suggest that Fe_7C_3 is a likely candidate component of the Earth's inner core. However, all of these conclusions are based on extrapolations of observations at temperatures and pressures much

lower than inner core conditions and they should, therefore, be treated with some caution. To investigate whether the properties of Fe_7C_3 are truly a match for the inner core, we have performed ab initio molecular dynamics (AIMD) simulations on Fe_7C_3 up to its melting temperature. Although the calculated elastic properties, including wave velocities, agree well with those from seismology, we find that the density of Fe_7C_3 is far too low for the inner core to be composed predominantly of this phase.

2. The Structure of Iron Carbides at Core Conditions

Although the Fe-C system is well understood at ambient pressures, studies targeted at determining the Fe-C phase diagram and crystal structures at higher pressures for geophysical applications are scarce and the thermodynamic stability and crystal structure of Fe_7C_3 at high temperatures and pressures are still under debate.

Observations from experiments are contradictory. *Rouquette et al*. [2008] saw stability of Fe_3C (space group Pnma) in the Fe-C system at 2200–3400 K and 25–70 GPa using a multianvil press (MAP) and laser-heated diamond anvil cell (LHDAC). *Nakajima et al*. [2011], however, observed the stability of Fe_7C_3 (space group $P6_3mc$) up to 71.5 GPa and 1973 K by carrying out in situ X-ray diffraction experiments, again using a MAP and a LHDAC.

Computational studies using both the random sampling [*Weerasinghe et al*., 2011] and evolutionary structure prediction algorithms [*Bazhanova et al*., 2012] based on enthalpy ranking predicted that both Fe_3C and Fe_7C_3 were thermodynamically unstable with respect to Fe_2C (space group *Pnma*) at inner core pressures ($T = 0$). However, when temperature is included, *Fei and Brosh* [2014] suggest stability of Fe_7C_3 at the ICB conditions by calculating the phase diagrams employing CALPHAD (CALculation of PHAse Diagrams), a thermodynamic database approach.

The crystal structure of Fe_7C_3 is also uncertain. The space group of Fe_7C_3 determined from experiments has long been assigned to $P6_3mc$, and the structure search by *Bazhanova et al*. [2012] also confirmed that this hexagonal (*h*) symmetry is more favorable than a structure with space group *Pnma* at ambient pressure. However, *Prescher et al*. [2015] observed another symmetry, *Pbca*, in all their multianvil experiments conducted at pressures from 7 to 15 GPa and temperatures from 1473 to 1973 K, and hence, their structure was denoted as *o*-Fe_7C_3 (*o* for orthorhombic). The three structures are very similar, and they are all constructed from CFe_6 trigonal prisms. Groups of three prisms are connected via shared vertices to form a triad; the triads are then linked into columns and the different polytypes are produced by variations in the packing of the columns. The structures can therefore be considered as having evolved from the same structural motif linked together in subtly different ways [*Prescher et al*., 2015].

In our present study, we used the $P6_3mc$ structure. It should, however, be noted that any of the three proposed structures should give comparable elastic properties due to their close structural similarity [*Mookherjee et al*., 2011; *Minobe et al*., 2015].

3. Methodology

3.1. Electronic Structure Calculations

The total energies and forces were calculated by solving the Schrödinger equation based on DFT, within the Vienna Ab Initio Simulation Package (VASP) code [*Kresse and Joubert*, 1999; *Blöchl*, 1994]. The electrons are described by single-particle wave functions with the interaction between them represented by an effective potential. The core-valence electron interaction is described by the projector augmented wave method [*Kresse and Furthmüller*, 1996a, 1996b; *Kresse and Hafner*, 1993]. The valence configurations Ar-$3d^6 4s^2$ and He-$2s^2 2p^2$ were used. Exchange-correlation effects were treated in the generalized gradient approximation with the Perdew, Burke, and Ernzerhof (PBE) scheme [*Perdew et al*., 1996]. As shown in previous studies, PBE works well for the description of the Fe-C system [*Mookherjee et al*., 2011; *Oganov et al*., 2013; *Raza et al*., 2015]. Both experiments [*Prescher et al*., 2015; *Chen et al*., 2014] and calculations [*Mookherjee et al*., 2011; *Raza et al*., 2015] show the disappearance of magnetic moments at high pressures (53 GPa *h*-Fe_7C_3 and 70 GPa for *o*-Fe_7C_3), so we performed nonspin polarized calculations for pressures above 70 GPa.

We ran finite temperature Born-Oppenheimer AIMD to verify the structure and calculate properties. The integration of the classical Newton's equations of motion uses the Verlet algorithm, and the ground state search is done within an efficient iterative matrix diagonalization scheme and a Pulay mixer for each step. A time

step of 1.0 fs was chosen for the integration. Simulations were performed at constant temperatures using an Andersen thermostat, with a restarting value of no less than 200 cycles.

The simulation box used to determine the elastic constants contained 40 atoms of the hexagonal Fe_7C_3 structure *h*-Fe_7C_3, which is $1\times1\times2$ supercell of the unit cell used in *Mookherjee et al*. [2011] and *Oganov et al*. [2013]. A **k**-point grid of eight irreducible **k** points and a plane-wave energy cutoff of 520 eV were required to obtain convergence in the energy and forces. A larger supercell ($2\times2\times2$) of 160 atoms was also used to verify the results from the 40 atom supercell; for these simulations a single $\mathbf{\Gamma}$ point and a cutoff energy of 400 eV were used.

Simulations were performed at temperatures between 0 and ~7000 K for between 8 and 15 ps. The temperature of the simulation was determined from a time average excluding the first 2 ps of the simulation. Stresses were determined as outlined below. To ensure that we were computing the stresses of solid phases, we retrieved the radial distribution function (RDF) and the root-mean-square displacements (RMSD) for the last 5 ps of each simulation.

3.2. Elastic Properties

In order to obtain the elastic properties at different pressures and temperatures, we first ran VASP-NPT simulations for the isothermal-isobaric ensemble, using the barostat implemented in VASP by Hernández [*Hernández*, 2001; *Souza and Martins*, 1997], to relax the unit cell parameters; these simulations were run for up to 12 ps. The lattice parameters obtained from these NPT simulations were then used to create unit cells to which distortions were applied (see below). The stresses on the simulation box were then obtained from NVT simulations run over 12 ps (8 ps for the 160 atom supercell); for simulations of the 40 atom supercell at target temperatures over 5000 K, 15 ps were used to ensure convergence.

The elastic moduli c_{ij} [*Simmons and Wang*, 1971] were evaluated using the stress-strain method. Two distortion matrices were applied to the relaxed equilibrium structure:

$$\begin{pmatrix} \mathbf{1}+\boldsymbol{\delta} & \mathbf{0} & \mathbf{0} \\ \mathbf{0} & \mathbf{1} & \boldsymbol{\delta}/\mathbf{2} \\ \mathbf{0} & \boldsymbol{\delta}/\mathbf{2} & \mathbf{1} \end{pmatrix} \quad \text{and} \quad \begin{pmatrix} \mathbf{1} & \mathbf{0} & \mathbf{0} \\ \mathbf{0} & \mathbf{1} & \mathbf{0} \\ \mathbf{0} & \mathbf{0} & \mathbf{1}+\boldsymbol{\delta} \end{pmatrix}.$$

Using the time-averaged stresses from the AIMD simulations, the elastic moduli were then obtained by the standard relation $\sigma_{ij}=c_{ijk}\cdot\varepsilon_{kl}$. Four different strains (±0.01 and ±0.02) were applied in each distortion and the resulting stress-strain values were then fitted to second-order polynomials; by evaluating the slopes at zero strain, the stress-strain relationship in the limit of equilibrium volume is then determined [*Karki et al*., 2001].

The statistical error in the temperature was evaluated using the blocking method for correlated data [*Flyvbjerg and Petersen*, 1989]. The standard deviation is defined as

$$\delta=\sqrt{\frac{c_0^{'}}{n^{'}-1}\left(1+\frac{1}{\sqrt{2(n^{'}-1)}}\right)}, \tag{1}$$

where $n'=n/2$, $c_0^{'}=\frac{1}{n}\sum_{k=1}^{n^{'}}(x_k-\overline{x})^2$, and $x_i^{'}=(x_{2i-1}+x_{2i})/2$; n is the number of data points and n' is created to fragment the data points. The final statistical error in temperature increases from 0.2 to 30 K as the temperature increases from 300 to 7000 K; this represents in all cases an error of less than 0.5%.

We used the Voigt average [*Simmons and Wang*, 1971] to evaluate the elastic properties (incompressibility: *K*; shear modulus: *G*):

$$K_T=[2(c_{11}+c_{12})+4c_{13}+c_{33}]/9 \tag{2}$$

$$G=(12c_{44}+7c_{11}-5c_{12}+2c_{33}-4c_{13})/30. \tag{3}$$

The adiabatic incompressibility, K_S is obtained from

$$K_S=K_T(1+\alpha\gamma T), \tag{4}$$

where α is the volumetric thermal expansion coefficient (5.8×10^{-6}/K, which was obtained from extrapolation of the unit cell volumes in *Nakajima et al*. [2011]). K_T is the isothermal bulk modulus, γ is the

Grüneisen parameter, and $\gamma_0 = 2.57$ [*Nakajima et al.*, 2011; *Mookherjee et al.*, 2011]. The volume dependence of γ is approximated from the experimental data with the relation [*Mookherjee et al.*, 2011]

$$\gamma(V) = \gamma_0 \left(\frac{V}{V_0}\right)^{2.2}. \tag{5}$$

The isotropic wave propagation velocities in the material can then be evaluated from the bulk and shear moduli and the density, ρ, as follows

$$V_P = \sqrt{\frac{K + \frac{4}{3}G}{\rho}} \tag{6}$$

and

$$V_S = \sqrt{\frac{G}{\rho}}. \tag{7}$$

The Debye sound velocity V_D has the relationship with V_P and V_S:

$$\frac{1}{V_D^3} = \frac{1}{V_P^3} + \frac{2}{V_S^3}. \tag{8}$$

The Poisson's ratio is obtained by

$$v = \frac{3K_S - 2G}{6K_S + 2G}. \tag{9}$$

3.3. Temperature Dependence of the Shear Modulus

We used the Nadal-Le Poac (NP) shear modulus model [*Nadal and Le Poac*, 2003], based on Lindemann melting theory, to describe the temperature dependence of G at a fixed pressure. This takes the form

$$G(P,T) = \frac{1}{J(T)}\left[\left(G_0 + \frac{\partial G}{\partial P}\frac{P}{\sqrt[3]{\eta}}\right)\left(1 - \frac{T}{T_m}\right) + \frac{\rho}{Cm}k_b T\right], \tag{10}$$

where

$$C = \frac{(6\pi)^{\left(\frac{2}{3}\right)}}{3} f^2, \tag{11}$$

$$J(T) = 1 + \exp\left[-\frac{1 + \frac{1}{\zeta}}{1 + \frac{\zeta}{1 - \frac{T}{T_m}}}\right], \tag{12}$$

and

$$G_P = G_0 + \frac{\partial G}{\partial P}\frac{P}{\sqrt[3]{\eta}}. \tag{13}$$

In equations (10)–(13), G is the shear modulus, G_0 is the shear modulus at 0 K and 0 GPa, P is pressure, T is temperature, T_m is the melting temperature, ρ is the density, m is the averaged atomic mass, η is the compression defined as the ratio of the density at current conditions to the density at 0 K and 0 GPa, k_b is the Boltzmann constant, f is the Lindemann constant for the material, and ζ is a material parameter. Our results were fitted to this NP model with four adjustable parameters, namely, T_m, G_P, C, and ζ (G_P was taken as a constant as explained in *Martorell et al.* [2013b]). With this model we can obtain the melting temperature of the material and its Lindemann constant. This last value is in the range of 0.1–0.3 for most materials [*Nadal and Le Poac*, 2003].

4. Results and Discussion

4.1. Comparison Between Experiment and Theory

As shown in Table 1, our static calculations at zero pressure gave $K_T = 287$ GPa and $G = 95$ GPa for the non-magnetic phase (nm) in the Voigt approximation. Our elastic properties are in very good agreement with

Table 1. Elastic Properties and Density of Fe_7C_3 Under Different Temperatures T and Pressures P[a]

State	T(K)	P(GPa)	C_{11}(GPa)	C_{12}	C_{13}	C_{33}	C_{44}	K_T(GPa)	G(GPa)	ρ(g/cm)[3]	V_D(km/s)
fm	0	0	412	176	167	362	101	245	109	7.872	4.16
fm[b]	*0*	*0*	*397*	*173*	*168*	*247*	*102*	*223*	*102*	-	-
nm	0	0	448	199	215	427	60	287	95	8.137	3.85
nm[b]	*0*	*0*	*458*	*200*	*205*	*425*	*67*	*285*	*101*	-	-
nm	0	350	2107	1345	1384	1959	239	1599	309	12.523	5.63
nm	300	150	1187	714	759	1137	155	886	194	10.620	4.84
nm[c]	*300*	*158(5)*	-	-	-	-	-	*929(27)*	*221(11)*	*10.66(6)*	*5.151(122)*
nm[d]	*0*	*150*	-	-	-	-	-	*743*	*203*	*10.625*	-
nm	300	180	1390	842	905	1267	209	1039	231	10.956	5.20
nm	1760	85	859	537	447	651	58	616	118	9.569	3.98
nm[c]	*1800*	*85(2)*	-	-	-	-	-	*600(14)*	*132(8)*	*9.67(4)*	*4.175(114)*
								K_S(GPa)			
nm	1868	350	1902	1326	1320	1808	249	1544	267	12.380	5.27
nm	2850	350	1807	1279	1313	1765	267	1491	258	12.309	5.20
nm	4879	350	1769	1263	1291	1714	246	1483	243	12.126	5.08
nm	5395	350	1689	1262	1288	1690	230	1467	217	12.086	4.81
nm	5645	350	1664	1254	1247	1651	222	1436	212	12.075	4.76
nm	5921	350	1583	1223	1215	1599	224	1392	200	12.027	4.63
nm	6446	350	1230	966	1294	1687	131	1300	118	11.993	3.58
nm	6513	350	1169	886	1224	1624	45	1229	88	11.912	3.10
nm[e]	6022	350	1652	1233	1260	1667	193	1439	200	12.055	4.64
nm[e]	6169	350	1473	1158	1165	1631	169	1370	172	12.051	4.30

[a]Results for the simulations at the two highest temperatures are not shown as Fe_7C_3 melts after about 7 ps at 6670 K and melts immediately at 7055 K (see supporting information). fm and nm indicate ferromagnetism and nonmagnetism, respectively. Data from other studies are in italic text.
[b]*h*-Fe_7C_3, DFT-PBE calculation [*Mookherjee et al.*, 2011].
[c]*o*-Fe_7C_3, Experiment [*Prescher et al.*, 2015] the number in brackets indicates error.
[d]*o*-Fe_7C_3, DFT-PBE calculation [*Raza et al.*, 2015].
[e]The 160 atom supercell.

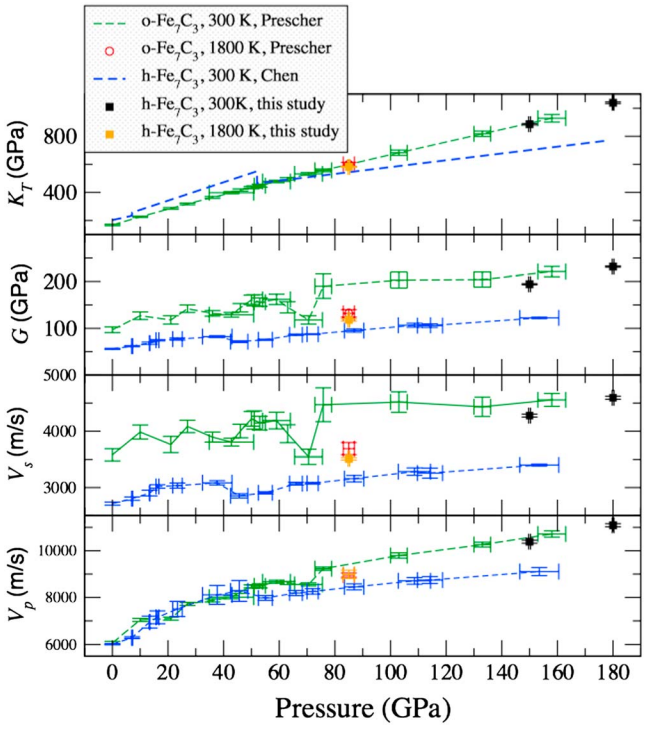

Figure 1. Comparison of our results for *h*-Fe_7C_3 with the experimental data of *Chen et al.* [2014] and *Prescher et al.* [2015] for G, K_T, V_P, and V_S.

those in *Mookherjee et al.* [2011], which gave $K_T = 285$ GPa and $G = 101$ GPa in the Voigt approximation. We also ran AIMD to compute finite temperature elasticity to compare with available experiments. At 300 K, our simulations at 150 GPa gave $K_T = 886$ GPa and $G = 194$ GPa, which agree well with the experimental data of *Prescher et al.* [2015], which gave $K_T = 929(27)$ GPa and $G = 221(11)$ at 158(5) GPa. A further calculation was performed at 1760 K and 85 GPa which gave similarly good agreement with the measurements of *Prescher et al.* [2015], $K_T = 616$ GPa and $G = 118$ GPa versus $K_T = 600(14)$ GPa and $G = 132(8)$ GPa.

Figure 1 shows our results for the hexagonal phase of Fe_7C_3 compared with available experimental data for both the hexagonal and orthorhombic phases [*Chen et al.*, 2014; *Prescher et al.*, 2015]. The experiments show that K_T and V_P of both phases are very similar below about 60 GPa, above

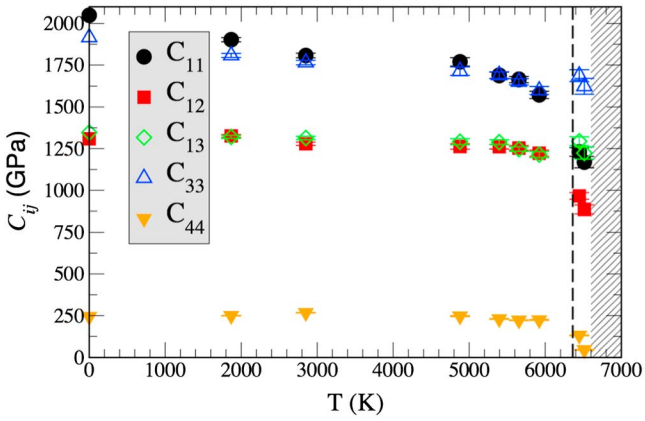

Figure 2. Calculated elastic constants for *h*-Fe_7C_3 as a function of simulation temperature at 350 GPa. The dashed line indicates the melting temperature of *h*-Fe_7C_3 from the NP model. The shaded region represents the melting temperatures of *hcp*-Fe [*Morard et al*., 2011]. The statistical errors are 0.68%, 0.77%, 1.42%, 1.12%, 1.12%, 1.49%, 2.06%, and 2.93% for temperatures of 1868, 2850, 4879, 5395, 5645, 5921, 6446, and 6513 K, respectively.

which the paramagnetic material becomes nonmagnetic, with a reduction in sound velocity observed by *Chen et al*. [2014] after the transition. Extrapolation by *Chen et al*. [2014] of their reduced velocities to core pressures suggests a match with seismic observations for the inner core; such a match is not, however, observed by *Prescher et al*. [2015] for the *o*-Fe_7C_3 phase, as their velocities are considerably higher. The difference in elastic properties between these two experimental studies may be due to the different equations of state used. While our calculations predict a density of 12.524 g/cm^3 at zero Kelvin and 350 GPa, that of *Chen et al*. [2012] is ~13.2 g/cm^3 at 300 K and 350 GPa. However, our results are in much better agreement with *Prescher et al*. [2015]. The calculated densities at 300 K, 150 GPa and 1760 K, 85 GPa are 10.620 and 9.569 g/cm^3, respectively, which match well with the experimental data of *Prescher et al*. [2015] for *o*-Fe_7C_3 (10.66 ± 0.06 and 9.67 ± 0.04 g/cm^3 for 300 K, 158 ± 5 GPa and 1800 ± 200 K, 85 ± 2 GPa, respectively). Our calculated elastic properties at both 300 K and 1760 K for *h*-Fe_7C_3 are also in excellent agreement with the experiments of *Prescher et al*. [2015] for *o*-Fe_7C_3, suggesting similar behavior of the *h*-Fe_7C_3 and *o*-Fe_7C_3 phases. It also can be seen from Figure 1 that, as expected, the effect of temperature on *G*, and thus on V_S, is significant.

4.2. Elasticity of Fe_7C_3 at Inner Core Conditions

The elastic moduli of *h*-Fe_7C_3 at 350 GPa as a function of temperature are shown in Figure 2 and in Table 1. They all show an almost linear variation with *T* below ~5800 K. C_{11} and C_{33} decrease with increasing temperature (similar in behavior to pure *hcp*-Fe), while C_{12} and C_{13} slightly decrease with increasing temperature (opposite behavior to pure *hcp*-Fe). The shear stiffness modulus C_{44} shows little dependency on temperature below 6000 K. There is a crossover of C_{11} and C_{33} in *h*-Fe_7C_3 for temperatures approaching 6000 K.

Above 5800 K, C_{13} and C_{33} show a similar trend as before, though the scatter becomes large. However, C_{11}, C_{12}, and C_{44} show a significant nonlinear decrease with increasing temperature. In particular, from 6000 K to 6500 K, C_{11}, C_{12}, and C_{44} drop by 22%, 21%, and 42%, respectively. This behavior is similar to the premelting phenomenon found in pure *hcp*-Fe. Despite this premelting weakening, by analyzing the RDFs and RMSDs of the system, we found that Fe_7C_3 remained completely solid during the simulation to 6513 K; at 6670 K it melted after ~7 ps and melted immediately by 7055 K (Figure S1 in the supporting information).

The bulk and shear moduli (Figure 3) decrease almost linearly with increasing temperature up to ~5800 K, above which there is an abrupt and significant increase in the rate of reduction. We used the NP model [*Nadal and Le Poac*, 2003] to fit the temperature dependence of our shear modulus. The NP model is the only available model that accounts for both the linear region and the region close to the melting temperature, which has successfully described the nonlinear *T* dependency of *G* in tin [*Nadal and Le Poac*, 2003] and *hcp*-Fe [*Martorell et al*., 2013b]. We obtained a value of the Lindemann coefficient $f = 0.174$ and a melting temperature of 6470 K for *h*-Fe_7C_3 at 350 GPa. This calculated Lindemann coefficient seems reasonable since it is a material-dependent parameter that is normally in the range between 0.1 and 0.3 [*Nelson*, 2002].

4.3. Premelting Effects in Fe_7C_3

Our premelting in Fe_7C_3 occurs when $T/T_m > 0.93$, a slightly lower homologous temperature than was found in pure *hcp*-Fe [*Martorell et al*., 2013b] and in tin [*Nadal and Le Poac*, 2003]. As shown in Figure 3, the Poisson's

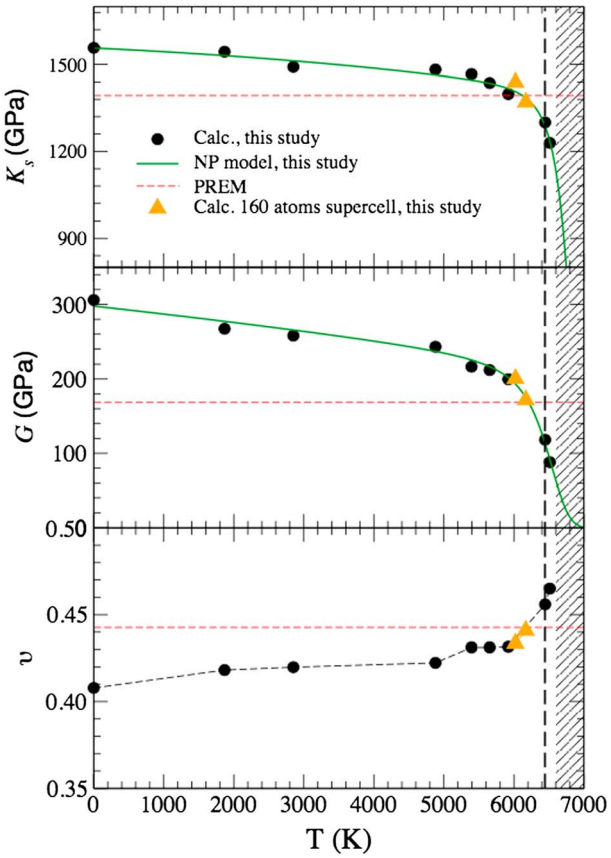

Figure 3. Calculated elastic moduli and Poisson's ratio for h-Fe_7C_3 as a function of simulation temperature at 350 GPa. The green line is the NP (NP-like) model fitted to the calculated shear (bulk) modulus. The dashed line indicates the melting temperature of h-Fe_7C_3. The horizontal dashed line is the value from PREM at 350 GPa [*Dziewonski and Anderson*, 1981]. The shaded region represents the melting temperatures of *hcp*-Fe [*Morard et al.*, 2011].

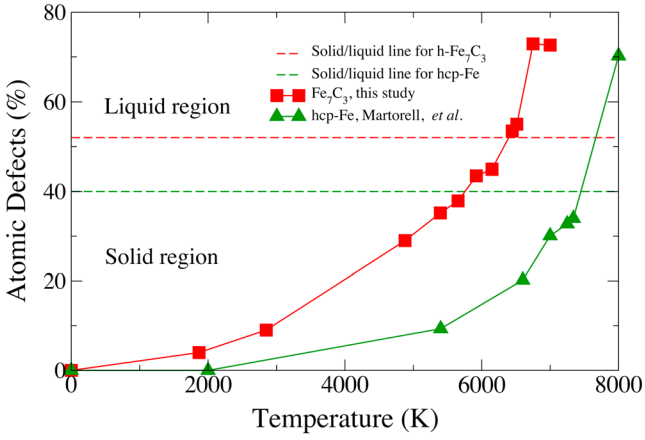

Figure 4. Atomic defects evolution of h-Fe_7C_3 only Fe atoms considered as a function of simulation temperature at 350 GPa in comparison with *hcp*-Fe [*Martorell et al.*, 2013b].

ratio also reveals a strong premelting effect approaching the melting point. The shear modulus, bulk modulus, and Poisson's ratio all cross the preliminary reference Earth model (PREM) value at temperatures between 6000 K and the melting point.

As well as premelting being evident in the elastic properties of Fe_7C_3, heating reveals a rapid increase in defects (defined as overcoordinated or undercoordinated atoms), as previously reported for pure *hcp*-Fe [*Martorell et al.*, 2013b]. However, the increase of defects in h-Fe_7C_3 is at a much faster rate (Figure 4), reaching ~52% before melting. The defect percentage at melting is higher than that found in elemental systems [*Delogu*, 2006a, 2006b; *Manai and Delogu*, 2007b; *Martorell et al.*, 2013b], a difference probably caused by the lower symmetry of the h-Fe_7C_3 structure, which allows significant mobility of the light carbon atoms sitting in the prismatic centers of the iron substructure.

4.4. Implications for Carbon in the Earth's Core

Figure 5 shows the dependence of V_P and V_S on temperature at 350 GPa. Both exhibit a similar trend to that of the shear and bulk moduli, decreasing almost linearly with temperature up to ~5800 K, followed by a substantial increase in the rate of reduction in wave velocities beyond this point. Our results from a fitted NP-like model show that the velocities agree with the seismological values at T/T_m of 0.984 and 0.966 (6370 K for V_P and 6250 K for V_S), respectively. The elastic constants of h-Fe_7C_3 (Figure 2) exhibit anisotropic behavior at the inner core conditions consistent with that found for the inner core from seismology [*Deuss*, 2014].

However, even at 0 K, the density of h-Fe_7C_3 (Figure 5) is much lower than the seismological values and the further, almost linear, reduction in its density with increasing temperature then gives a density mismatch between Fe_7C_3 and the inner core of 7.9% at

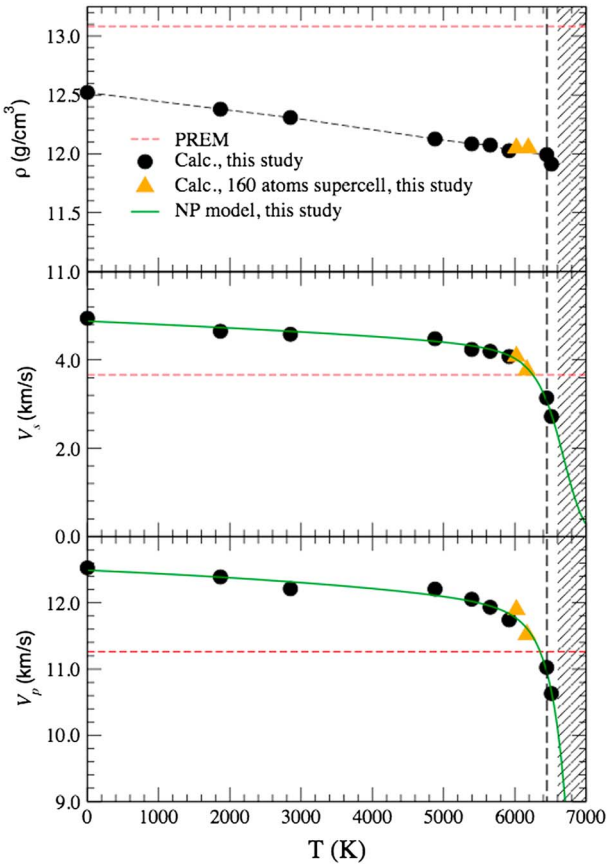

Figure 5. Calculated sound velocities and density for h-Fe_7C_3 as a function of simulation temperature at 350 GPa. The green line is the NP-like model fitted to the calculated sound velocities. The dashed line indicates the melting temperature of h-Fe_7C_3. The horizontal dashed line is the value from PREM at 350 GPa [*Dziewonski and Anderson*, 1981]. The shaded region represents the melting temperatures of *hcp*-Fe [*Morard et al.*, 2011].

6000 K. For this reason, we can exclude the possibility that the major phase in the Earth's inner core is h-Fe_7C_3 and probably also that carbon is the sole light element candidate present, although, of course the presence of Fe_7C_3 as a minor constituent is not precluded. It is interesting to note that similar arguments apply in the case of Fe_3C [e.g., *Vočadlo et al.*, 2002], in which the density was also found to be too low to match the inner core. In this case, however, the discrepancy was not so large (~3%), reflecting the lower carbon content. Of course, the presence of any amount of an Fe_7C_3 phase depends on the position of the high P/T eutectic, as well as the amount of carbon in the core; both of these are presently unknown. For small amounts of carbon expected in the core, this would require the eutectic to be very close to the iron-enriched side of the phase diagram.

The melting temperature from the NP model is 6470 K at 350 GPa for h-Fe_7C_3. The true melting temperature will be ~5500 K if we assume 15% overestimation due to overheating [*Martorell et al.*, 2013b; *Delogu*, 2006a, 2006b; *Lu and Li*, 1998; *Manai and Delogu*, 2007a]. This value suggests that the melting temperature of h-Fe_7C_3 may not be as high as previously expected (~6400 K from extrapolation of experimental data to 330 GPa) [*Fei and Brosh*, 2014]. If h-Fe_7C_3 really does have such a low melting temperature, it is also difficult to see how it would exist in equilibrium with *hcp*-Fe under inner core conditions, unless in the form of an impurity within an *hcp*-Fe superlattice.

5. Conclusions

We have studied the elastic properties of h-Fe_7C_3 at 350 GPa up to 7000 K. The sound velocities of Fe_7C_3 are very similar to those of PREM due to the premelting behavior of Fe_7C_3 just prior to melting. However, the density of h-Fe_7C_3 is 7.9% lower than the PREM value, and the estimated melting temperature is also very low compared to that of *hcp*-Fe. We conclude, therefore, that carbon within Fe_7C_3 alone is not a viable candidate for the major light element phase in the Earth's core. Whether carbon may exist as an impurity in *hcp*-Fe has yet to be determined.

Acknowledgments
This work was supported by NERC grant NE/M015181/1. Calculations were performed using the ARCHER supercomputer facility. Y. L. thanks Roberto Scipioni for the help with calculations. Supporting information is included as one table and one figure in the supporting information file; the source code (VASP) used in this study is available at https://www.vasp.at/. Both the data and input files necessary to reproduce the experiments with VASP are available from the authors upon request (yunguo.li@ucl.ac.uk).

References

Alboussière, T., R. Deguen, and M. Melzani (2010), Melting-induced stratification above the Earth's inner core due to convective translation, *Nature*, *466*(7307), 744–747.
Alfè, D., M. Gillan, and G. Price (2002), Composition and temperature of the Earth's core constrained by combining ab initio calculations and seismic data, *Earth Planet. Sci. Lett.*, *195*(1), 91–98.
Alfè, D., M. Gillan, and G. Price (2007), Temperature and composition of the Earth's core, *Contemp. Phys.*, *48*(2), 63–80.
Allègre, C. J., J.-P. Poirier, E. Humler, and A. W. Hofmann (1995), The chemical composition of the Earth, *Earth Planet. Sci. Lett.*, *134*(3), 515–526.
Badro, J., A. S. Côté, and J. P. Brodholt (2014), A seismologically consistent compositional model of Earth's core, *Proc. Natl. Acad. Sci. U.S.A.*, *111*(21), 7542–7545.

Bazhanova, Z. G., A. R. Oganov, and O. Gianola (2012), Fe-C and Fe-H systems at pressures of the Earth's inner core, *Phys. Usp.*, *55*(5), 489–497.
Belonoshko, A. B., N. V. Skorodumova, S. Davis, A. N. Osiptsov, A. Rosengren, and B. Johansson (2007), Origin of the low rigidity of the Earth's inner core, *Science*, *316*(5831), 1603–1605.
Birch, F. (1952), Elasticity and constitution of the Earth's interior, *J. Geophys. Res.*, *57*, 227–286, doi:10.1029/JZ057i002p00227.
Blöchl, P. E. (1994), Projector augmented-wave method, *Phys. Rev. B*, *50*(24), 17953.
Chen, B., L. Gao, B. Lavina, P. Dera, E. E. Alp, J. Zhao, and J. Li (2012), Magneto-elastic coupling in compressed Fe_7C_3 supports carbon in Earth's inner core, *Geophys. Res. Lett.*, *39*, L18301, doi:10.1029/2012GL052875.
Chen, B., et al. (2014), Hidden carbon in Earth's inner core revealed by shear softening in dense Fe_7C_3, *Proc. Natl. Acad. Sci. U.S.A.*, *111*(50), 17,755–17,758.
Delogu, F. (2006a), Homogeneous melting of metals with different crystalline structure, *J. Phys. Condens. Matter*, *18*(24), 5639.
Delogu, F. (2006b), Mechanistic aspects of homogeneous and heterogeneous melting processes, *J. Phys. Chem. B*, *110*(25), 12,645–12,652.
Deuss, A. (2014), Heterogeneity and anisotropy of Earth's inner core, *Annu. Rev. Earth Planet. Sci.*, *42*, 103–126.
Dziewonski, A. M., and D. L. Anderson (1981), Preliminary reference Earth model, *Phys. Earth Planet. Inter.*, *25*(4), 297–356.
Fei, Y., and E. Brosh (2014), Experimental study and thermodynamic calculations of phase relations in the Fe–C system at high pressure, *Earth Planet. Sci. Lett.*, *408*, 155–162.
Flyvbjerg, H., and H. G. Petersen (1989), Error estimates on averages of correlated data, *J. Chem. Phys.*, *91*(1), 461–466.
Hernández, E. (2001), Metric-tensor flexible-cell algorithm for isothermal–isobaric molecular dynamics simulations, *J. Chem. Phys.*, *115*(22), 10,282–10,290.
Hillgren, V., C. Gessmann, and J. Li (2000), An experimental perspective on the light element in Earth's core, in *Origin of the Earth and Moon*, vol. 30, pp. 245–263, Univ. of Arizona Press, Tucson.
Huang, H., Y. Fei, L. Cai, F. Jing, X. Hu, H. Xie, L. Zhang, and Z. Gong (2011), Evidence for an oxygen-depleted liquid outer core of the Earth, *Nature*, *479*(7374), 513–516.
Karki, B. B., L. Stixrude, and R. M. Wentzcovitch (2001), High-pressure elastic properties of major materials of Earth's mantle from first principles, *Rev. Geophys.*, *39*, 507–534, doi:10.1029/2000RG000088.
Kresse, G., and J. Furthmüller (1996a), Efficiency of ab-initio total energy calculations for metals and semiconductors using a plane-wave basis set, *Comput. Mater. Sci.*, *6*(1), 15–50.
Kresse, G., and J. Furthmüller (1996b), Efficient iterative schemes for ab initio total-energy calculations using a plane-wave basis set, *Phys. Rev. B*, *54*(16), 11,169.
Kresse, G., and J. Hafner (1993), Ab initio molecular dynamics for open-shell transition metals, *Phys. Rev. B*, *48*(17), 13,115.
Kresse, G., and D. Joubert (1999), From ultrasoft pseudopotentials to the projector augmented-wave method, *Phys. Rev. B*, *59*(3), 1758.
Lord, O., M. Walter, R. Dasgupta, D. Walker, and S. Clark (2009), Melting in the Fe–C system to 70 GPa, *Earth Planet. Sci. Lett.*, *284*(1), 157–167.
Lu, K., and Y. Li (1998), Homogeneous nucleation catastrophe as a kinetic stability limit for superheated crystal, *Phys. Rev. Lett.*, *80*(20), 4474.
Manai, G., and F. Delogu (2007a), Homogeneous and heterogeneous melting behavior of bulk and nanometer-sized Cu systems: A numerical study, *J. Mater. Sci.*, *42*(16), 6672–6683.
Manai, G., and F. Delogu (2007b), Numerical simulations of the melting behavior of bulk and nanometer-sized Cu systems, *Physica B*, *392*(1), 288–297.
Martorell, B., J. Brodholt, I. G. Wood, and L. Vočadlo (2013a), The effect of nickel on the properties of iron at the conditions of Earth's inner core: Ab initio calculations of seismic wave velocities of Fe–Ni alloys, *Earth Planet. Sci. Lett.*, *365*, 143–151.
Martorell, B., L. Vočadlo, J. Brodholt, and I. G. Wood (2013b), Strong premelting effect in the elastic properties of *hcp*-Fe under inner-core conditions, *Science*, *342*(6157), 466–468.
McDonough, W. F., and S.-S. Sun (1995), The composition of the Earth, *Chem. Geol.*, *120*(3), 223–253.
Minobe, S., Y. Nakajima, K. Hirose, and Y. Ohishi (2015), Stability and compressibility of a new iron-nitride-Fe_7N_3 to core pressures, *Geophys. Res. Lett.*, *42*, 5206–5211, doi:10.1002/2015GL064496.
Mookherjee, M., Y. Nakajima, G. Steinle-Neumann, K. Glazyrin, X. Wu, L. Dubrovinsky, C. McCammon, and A. Chumakov (2011), High-pressure behavior of iron carbide (Fe_7C_3) at inner core conditions, *J. Geophys. Res.*, *116*, B04201, doi:10.1029/2010JB007819.
Morard, G., J. Bouchet, D. Valencia, S. Mazevet, and F. Guyot (2011), The melting curve of iron at extreme pressures: Implications for planetary cores, *High Energy Density Phys.*, *7*(3), 141–144.
Nadal, M.-H., and P. Le Poac (2003), Continuous model for the shear modulus as a function of pressure and temperature up to the melting point: Analysis and ultrasonic validation, *J. Appl. Phys.*, *93*(5), 2472–2480.
Nakajima, Y., E. Takahashi, T. Suzuki, and K. I. Funakoshi (2009), "Carbon in the core" revisited, *Phys. Earth Planet. Inter.*, *174*, 202–211.
Nakajima, Y., E. Takahashi, N. Sata, Y. Nishihara, K. Hirose, K. Funakoshi, and Y. Ohishi (2011), Thermoelastic property and high-pressure stability of Fe_7C_3: Implication for iron-carbide in the Earth's core, *Am. Mineral.*, *96*(7), 1158–1165.
Nelson, D. R. (2002), *Defects and Geometry in Condensed Matter Physics*, Cambridge Univ. Press, Cambridge.
Oganov, A. R., R. J. Hemley, R. M. Hazen, and A. P. Jones (2013), Structure, bonding, and mineralogy of carbon at extreme conditions, *Rev. Mineral. Geochem.*, *75*(1), 47–77.
Olson, P., and R. Deguen (2012), Eccentricity of the geomagnetic dipole caused by lopsided inner core growth, *Nat. Geosci.*, *5*(8), 565–569.
Perdew, J. P., K. Burke, and M. Ernzerhof (1996), Generalized gradient approximation made simple, *Phys. Rev. Lett.*, *77*(18), 3865–3868.
Poirier, J.-P. (1994), Light elements in the Earth's outer core: A critical review, *Phys. Earth Planet. Inter.*, *85*(3), 319–337.
Prescher, C., et al. (2015), High Poisson's ratio of Earth's inner core explained by carbon alloying, *Nat. Geosci.*, *8*(3), 220–223.
Raza, Z., N. Shulumba, N. M. Carrey, L. Dubrovinsky, and I. A. Abrikosov (2015), First-principles calculations of properties of orthorhombic iron carbide Fe_7C_3 at the Earth's core conditions, *Phys. Rev. B*, *91*(21), 214112.
Rouquette, J., D. Dolejs, I. Y. Kantor, C. McCammon, D. Frost, V. Prakapenka, and L. Dubrovinsky (2008), Iron-carbon interactions at high temperatures and pressures, *Appl. Phys. Lett.*, *92*(12), 121912.
Simmons, G., and H. Wang (1971), *Single Crystal Elastic Constants and Calculated Aggregate Properties: A Handbook*, MIT Press, Cambridge, Mass.
Souza, I., and J. Martins (1997), Metric tensor as the dynamical variable for variable-cell-shape molecular dynamics, *Phys. Rev. B*, *55*(14), 8733.
Tkalčić, H. (2015), Complex inner core of the Earth: The last frontier of global seismology, *Rev. Geophys.*, *53*, 59–94, doi:10.1002/2014RG000469.
Vočadlo, L. (2007), Ab initio calculations of the elasticity of iron and iron alloys at inner core conditions: Evidence for a partially molten inner core?, *Earth Planet. Sci. Lett.*, *254*(1), 227–232.
Vočadlo, L., J. Brodholt, D. P. Dobson, K. Knight, W. Marshall, G. D. Price, and I. G. Wood (2002), The effect of ferromagnetism on the equation of state of Fe_3C studied by first-principles calculations, *Earth Planet. Sci. Lett.*, *203*(1), 567–575.

Vočadlo, L., D. P. Dobson, and I. G. Wood (2009), Ab initio calculations of the elasticity of *hcp*-Fe as a function of temperature at inner-core pressure, *Earth Planet. Sci. Lett.*, *288*(3), 534–538.

Wang, T., X. Song, and H. H. Xia (2015), Equatorial anisotropy in the inner part of Earth's inner core from autocorrelation of earthquake coda, *Nat. Geosci.*, *8*(3), 224–227.

Weerasinghe, G. L., R. Needs, and C. J. Pickard (2011), Computational searches for iron carbide in the Earth's inner core, *Phys. Rev. B*, *84*(17), 174110.

Wood, B. J., J. Li, and A. Shahar (2013), Carbon in the core: Its influence on the properties of core and mantle, *Rev. Mineral. Geochem.*, *75*, 231–250.